Original Article | Open Access

Plastic and Aesthetic Research

Ren et al. Plast Aesthet Res. 2026;13:34 DOI:10.20517/2347-9264.2026.121

Portable optical coherence tomography for monitoring artificial dermal scaffold integration: a murine and clinical study

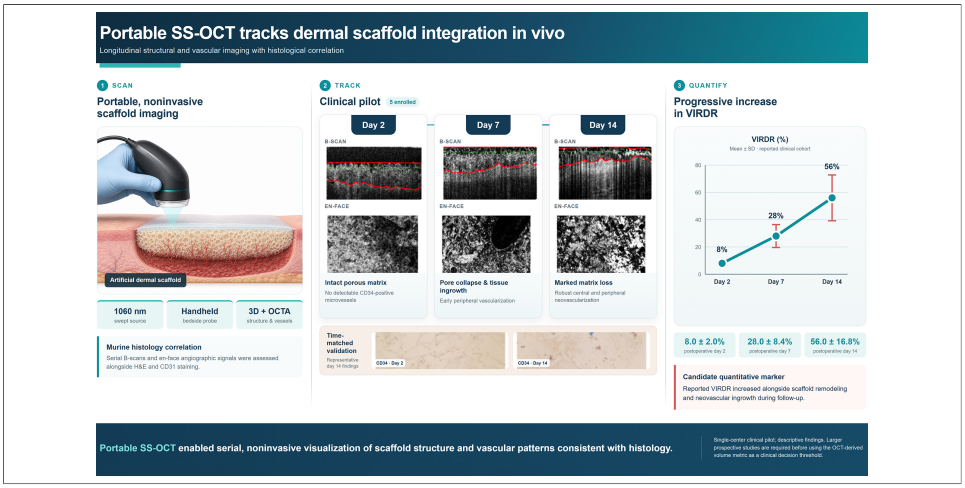
Zhiyang Ren[1], Shuhan Tang[2], Yao Xu[1], Yasen Cui[1], Jianhua Mo[3], Ke Li[1]

Keywords:
Full-thickness skin defect, artificial dermal scaffold, optical coherence tomography

Citation: Ren Z, Tang S, Xu Y, Cui Y, Mo J, Li K. Portable optical coherence tomography for monitoring artificial dermal scaffold integration: a murine and clinical study. *Plast Aesthet Res.* 2026;13:34. https://dx.doi.org/10.20517/2347-9264.2026.121

Received: 12 Aug 2026 **First Decision:** 20 Sep 2026 **Revised:** 22 Oct 2026 **Accepted:** 13 Nov 2026 **Published:** 18 Nov 2026

Academic Editor: Pietro Gentile
Copy Editor: Ting-Ting Hu
Production Editor: Ting-Ting Hu



Abstract

Aim: To develop a handheld swept-source optical coherence tomography (SS-OCT) system, assess the correspondence between OCT and histological findings in murine wounds, and evaluate its clinical applicability in patients treated with artificial dermal scaffolds.

Methods: A full-thickness wound model was established in 30 male ICR mice. Lando artificial dermal scaffolds or autologous skin grafts were implanted with or without basic fibroblast growth factor (bFGF). Structural brightness-scan (B-scan) images and en face optical coherence tomography (OCT) angiographic projections were acquired longitudinally and compared with hematoxylin and eosin (H&E) staining and cluster of differentiation 31 (CD31, platelet endothelial cell adhesion molecule-1) immunohistochemistry. Clinical validation included five patients with full-thickness skin defects reconstructed using bilayer Lando scaffolds. Serial SS-OCT findings were compared with H&E staining and cluster of differentiation 34 (CD34) immunohistochemistry. The collagen sponge layer was segmented to calculate the Index of Scaffold Ingrowth, Vascularization and Degradation (IRDR) from the relative reduction in volume.

Check for updates

[1]Department of Burn and Plastic Surgery, The First Affiliated Hospital of Soochow University, Soochow University, Suzhou 215006, Jiangsu, China.
[2]Suzhou Medical College of Soochow University, Soochow University, Suzhou 215123, Jiangsu, China.
[3]School of Electronics and Information Engineering, Soochow University, Suzhou 215123, Jiangsu, China.

Correspondence to: Dr. Ke Li, Department of Burn and Plastic Surgery, The First Affiliated Hospital of Soochow University, Soochow University, Suzhou 215006, Jiangsu, China. Email: like1234@suda.edu.cn

Results: In mice, OCT features corresponded to sequential histological changes, from inflammatory infiltration to matrix formation and neovascularization. The bFGF-treated scaffold group showed earlier and more pronounced vascular signals. In patients, SS-OCT images showed close visual agreement with histopathological findings, and the estimated IRDR of the collagen sponge layer increased progressively during follow-up.

Conclusion: Portable SS-OCT provides repeatable, non-invasive *in vivo* structural and vascular imaging that corresponds to histological findings in murine and human wounds. SS-OCT shows promise for longitudinal monitoring of artificial dermal scaffold integration and may help optimize dressing-change intervals and the timing of second-stage grafting.

INTRODUCTION

Full-thickness skin defects commonly require reconstruction following trauma, burns, tumor excision, or surgery[1,2]. Available approaches include direct closure, skin grafting, flap reconstruction, and tissue expansion[3,4]. Split-thickness skin grafting is widely used because it is technically straightforward and limits donor-site morbidity[5-8]. However, a thin graft placed directly on a wound bed lacking dermis is prone to secondary contraction and conspicuous scarring, which can impair function and appearance. Reconstructing a vascularized dermal layer can improve graft take and provide a template for more organized tissue repair.

Artificial dermal scaffolds are porous, biocompatible, biodegradable matrices used to reconstruct wounds resulting from burns, mechanical trauma, tumor resection, and scar revision[9-13]. Bilayer products combine a temporary silicone epidermal barrier with a collagen sponge that supports cell migration and vascular ingrowth. Treatment is typically staged: scaffold implantation is followed by removal of the silicone layer and placement of a split-thickness autograft once the neodermis has matured[14]. The conventional "three observations and one press" assessment relies on subjective judgments of wound color, separation between the silicone and collagen layers, scaffold adherence to the wound bed, and blanching under compression; it lacks standardized quantitative criteria. Although biopsy permits histological verification, it is invasive, samples only a limited area of tissue, and is unsuitable for repeated bedside monitoring[15,16].

Optical coherence tomography (OCT) provides label-free, depth-resolved imaging by detecting interference between reference light and light backscattered from tissue. Since its first demonstration in retinal imaging in 1991[17], OCT has been applied to dermatology and wound imaging, where it can resolve epidermal and dermal architecture and, through motion-contrast processing, microvascular changes[18-21]. These capabilities make OCT well suited to repeated assessment of scaffold-wound apposition, collagen sponge architecture, tissue ingrowth, and vascularization without disturbing the wound.

We therefore developed a portable handheld swept-source optical coherence tomography (SS-OCT) system for longitudinal monitoring of artificial dermal scaffolds. In the murine model, structural brightness-scan (B-scan) images, en face projections, and OCT angiographic features were compared with hematoxylin and eosin (H&E) staining and cluster of differentiation 31 (CD31) immunohistochemistry to assess inflammation, scaffold remodeling, and neovascularization. The same imaging approach was then applied to patients receiving artificial dermal scaffolds, with complementary validation using H&E staining, cluster of differentiation 34 (CD34) immunohistochemistry, and the Index of Scaffold Ingrowth, Vascularization and Degradation (IRDR). Clinical evaluation supported the feasibility of safe, non-invasive longitudinal monitoring of artificial dermal scaffolds in humans. The quantitative IRDR index provides an objective measure of scaffold degradation that may help address the subjectivity of conventional visual inspection.

This approach offers quantitative imaging information to support individualized wound management and the timing of reconstruction in burn and plastic surgery. The study had two main objectives: (i) to verify the feasibility of longitudinal, non-invasive *in vivo* monitoring of artificial dermal scaffolds using SS-OCT; and (ii) to apply IRDR clinically as a potential quantitative imaging biomarker to inform dressing-change intervals and the timing of second-stage split-thickness skin grafting. These preliminary findings suggest that OCT may reduce some of the subjectivity and delays associated with conventional observational methods and serve as an adjunct to wound management after dermal scaffold reconstruction. Validation in larger cohorts is warranted.

METHODS

Animal preparation

Thirty male ICR mice aged 8-12 weeks were obtained from Shanghai Jihui Laboratory Animal Breeding Co., Ltd. [SCXK (Hu) 2022-0009] and housed in the barrier facility of the Experimental Center at Soochow University [SYXK (Su) 2021-0074]. Temperature was maintained at 20-26 °C and relative humidity at 40%-70%, with ad libitum access to sterilized feed and water. Experiments began after one week of acclimatization. For surgical procedures and OCT imaging, anesthesia was induced by intraperitoneal injection of 4% chloral hydrate at 100 μL/10 g body weight. Aseptic technique was used throughout.

All animal experiments were conducted in accordance with the Animal Research: Reporting of *In Vivo* Experiments (ARRIVE) 2.0 guidelines and approved by the Animal Ethics Committee of Soochow University (Ethics No.: SUDA20250415A01). Mice were randomly assigned to experimental subgroups using a random number generator. Investigators conducting qualitative histological assessments were blinded to group allocation. Postoperative analgesia consisted of subcutaneous buprenorphine (0.05 mg/kg) every 12 h for 3 consecutive days after wound creation. At the terminal endpoint, mice were deeply anesthetized with 4% chloral hydrate and euthanized by cervical dislocation. The animal sample size was based on practical experience from similar scaffold-imaging studies. No formal power calculation was performed because the murine outcomes were assessed descriptively.

Principle of OCT

OCT is an optical ranging method based on low-coherence interferometry[17,22,23]. A fiber coupler divides the swept-source light between a reference arm and a sample arm. For a reflector at optical path delay Δz, the detected spectrum contains a modulation that can be represented in simplified form as $I(k) = S(k)\,[Rr + Rs + 2\sqrt{(RrRs)}\cos(2k\Delta z + \varphi)]$, where k is wavenumber, S(k) is the source spectrum, Rr and Rs are the reference and sample reflectivities, and φ is phase. Interference is detected only for path delays within the source coherence range, providing depth selectivity while optical heterodyne detection amplifies weak backscatter from tissue.

In SS-OCT, the narrow instantaneous laser line is swept across a broad optical bandwidth, and the interference signal is sampled as a function of k. Following background removal, k-linearization, dispersion compensation, apodization, and Fourier transformation, the modulation frequency is mapped to depth and its amplitude to local backscattering strength. This generates an axial reflectivity profile, or amplitude-scan (A-scan), without mechanically translating the reference mirror. Axial resolution is governed primarily by the swept bandwidth [$\delta z \approx (2\ln 2 / \pi)(\lambda 0^2 / \Delta\lambda)$ for a Gaussian spectrum in air], whereas lateral resolution depends on the focused spot size and numerical aperture. Thus, the two resolutions are controlled by different system parameters. Figure 1 illustrates the schematic and hardware configuration of the SS-OCT system.

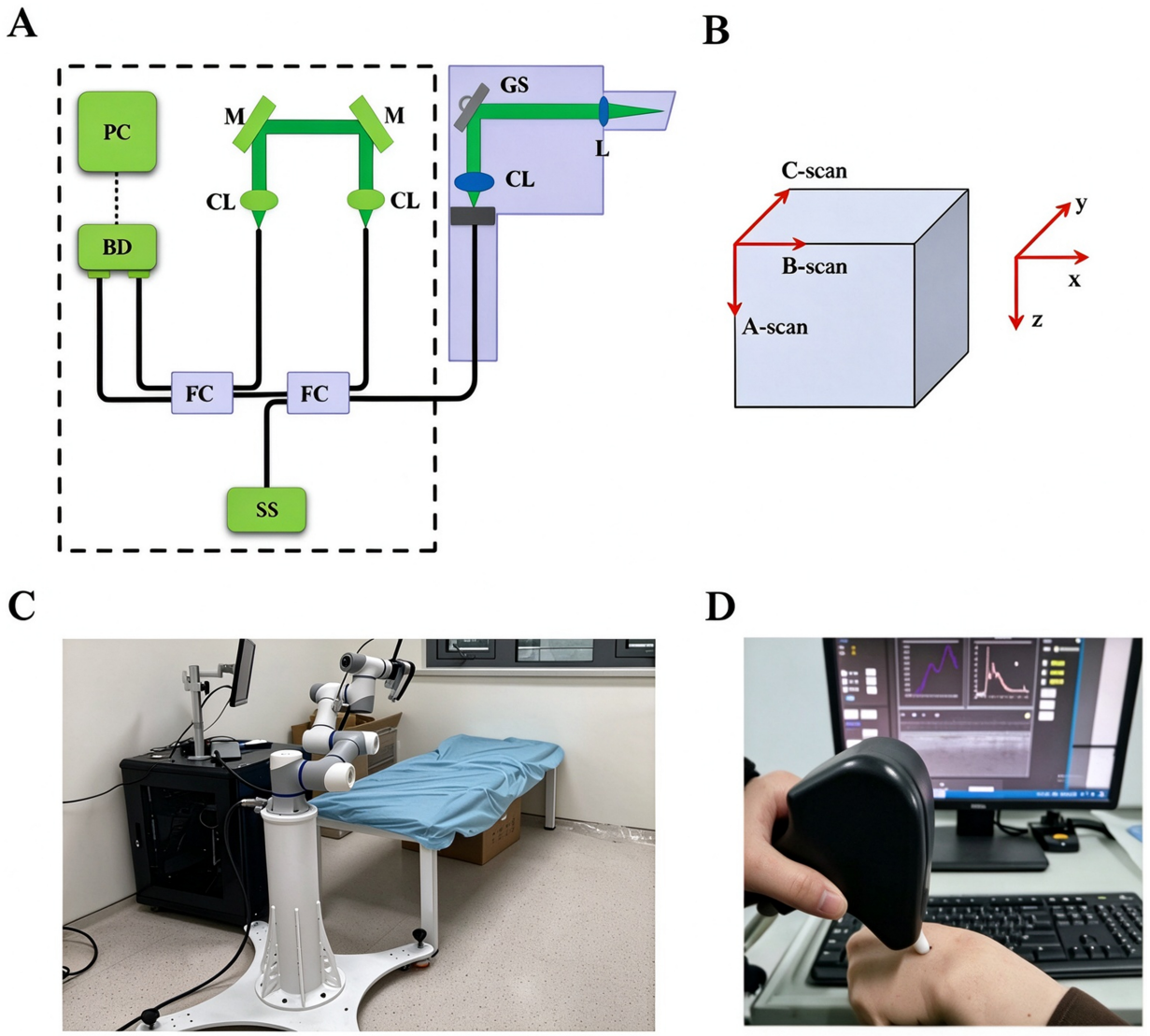


Figure 1. Schematic and setup of the OCT system. (A) Schematic illustrating the basic principles of OCT; (B) OCT scanning modes. A single scan along the depth direction (z-axis) is defined as an A-scan. A series of A-scans acquired along the lateral direction (x-axis) forms a two-dimensional cross-sectional B-scan; (C) Overview of the OCT instrument; (D) Photograph of the OCT system in operation. (C and D) are original photographs captured by the authors. OCT: Optical coherence tomography; A-scan: amplitude scan; B-scan: brightness scan.

The portable system used a Mach-Zehnder configuration and a 100 kHz swept source (SS-OCT1060, Axsun Technologies) centered near 1,060 nm with an approximately 1,000-1,100 nm sweep range. In the sample arm, light passed through a collimator (F280APC-1064, Thorlabs), a pair of galvanometer scanners (GVSM002/M, Thorlabs), and a focusing lens (AC254-060-B, Thorlabs). These components were integrated into a handheld probe with a disposable contact interface and an imaging window (WG10530-B, Thorlabs) tilted by 10° to reduce specular reflection. The reference arm used a fixed one-way optical path. Returning sample and reference light were recombined by a 50/50 fiber coupler and measured with a balanced photodetector (PDB471C, Thorlabs), which suppressed common-mode intensity noise before 12-bit digitization (ATS9351, AlazarTech).

Successive A-scans acquired along the x-axis formed cross-sectional B-scans. Sequential B-scans acquired along the orthogonal axis formed three-dimensional volumes, from which depth-selected en face projections were generated. Repeated B-scans acquired at the same location provided temporal signal variations that

served as motion contrast for OCT angiography. Branching en face signals were interpreted alongside CD31/CD34 staining rather than treated as independent histological evidence. The measured axial resolution was approximately 10.7 μm in air, the lateral resolution approximately 20 μm, and the imaging depth approximately 3.78 mm in air. A typical volume covered 2.8 mm × 2.8 mm, and the software displayed B-scans in real time to guide probe placement[24].

Image acquisition

OCT was the primary monitoring method in this study and was used for standardized, non-invasive, longitudinal *in vivo* imaging. Imaging began on postoperative day 3 and was repeated every other day, on days 3, 5, 7, 9, and 11, to monitor wound healing and changes in the scaffold. Images were acquired using the portable 1,060 nm SS-OCT system described above, with a handheld probe that allowed flexible positioning.

During *in vivo* imaging, mice were anesthetized and immobilized. The operator gently positioned the handheld OCT probe perpendicular to the target wound area to maintain a stable imaging distance and minimize motion artifacts. The imaging window, tilted by 10°, helped suppress specular reflection from the tissue surface. Two to three representative sites were selected within each wound, and 2-3 OCT volumes were acquired per site. The wound, imaging site, and acquisition date were recorded to facilitate longitudinal comparisons.

The acquired OCT signals were reconstructed into structural images and en face angiographic images. Structural OCT depicted the three-dimensional morphology of the wound and implanted scaffold, enabling assessment of scaffold degradation, tissue ingrowth, and structural changes. OCT angiography visualized changes in the vascular network within the scaffold region. Subsequent H&E staining and CD31 immunohistochemistry were used to compare OCT findings with microscopic pathological changes.

Animal experimental design

A standardized circular full-thickness skin defect, 15 mm in diameter, was created on the dorsum of each mouse. The epidermis, dermis, and part of the subcutaneous tissue were excised using sterile surgical scissors. After hemostasis, a Lando artificial dermal scaffold was trimmed to fit the wound, placed on the wound bed, and secured at the wound margins with 5-0 absorbable sutures. In the autologous skin graft groups, the excised full-thickness skin was trimmed, repositioned, and sutured onto the recipient wound bed. Thirty mice were allocated to a terminal histology cohort (n = 18) or a longitudinal imaging cohort (n = 12). The terminal histology cohort received a Lando artificial dermal scaffold with basic fibroblast growth factor (bFGF) (n = 9) or a Lando scaffold alone (n = 9). Within each treatment condition, three mice were assigned to tissue collection on each of postoperative days 3, 7, and 11 (n = 3 per condition per endpoint). The longitudinal imaging cohort was divided into four groups: Lando scaffold with bFGF, Lando scaffold alone, autologous skin graft with bFGF, and autologous skin graft alone (n = 3 per group). These mice were followed serially through postoperative day 11 without interim tissue collection.

Mice in the bFGF groups received perilesional injections of 0.3 mL of recombinant bovine bFGF topical solution (Beifuji; active ingredient concentration: 21,000 IU/mL; manufacturer: Zhuhai ESPOIR Biotech Co., Ltd.; catalog number: BFJ-01; batch number: 20240312). Injections were administered at 3-4 sites around the wound every two days. Although Beifuji is commercially formulated for topical application, perilesional injection was used in this study to achieve sustained local drug delivery to the surrounding tissue. A vehicle-only injection control was not included because repeated perilesional injections of a large volume of vehicle could increase the risk of tissue edema, local trauma, and wound disturbance, potentially confounding the results and disrupting normal wound healing. The potential confounding effect of the injection procedure is addressed further in the Discussion. The corresponding groups without bFGF received no drug intervention.

In the terminal histology cohort, OCT was performed immediately before tissue collection on postoperative days 3, 7, and 11. At each endpoint, wound tissue from three mice per condition was harvested for histopathological sectioning, H&E staining, and CD31 immunohistochemistry (n = 3 per condition per endpoint).

In the longitudinal imaging cohort, the same mice (n = 3 per group) underwent OCT imaging every other day on postoperative days 3, 5, 7, 9, and 11. At each session, 2-3 sites were selected within the wound, and 2-3 OCT volumes were acquired per site. The imaging location and date were recorded. OCT angiography was used to assess vascular growth within the scaffold or graft, while structural OCT was used to assess degradation of the implanted material, tissue regeneration, and graft integration.

Statistical analysis

Murine outcomes were analyzed descriptively because of the small sample size. Continuous clinical variables were summarized as the mean ± standard deviation (SD). Paired-samples t-tests were used to compare IRDR values across follow-up time points. A two-sided P-value < 0.05 was considered statistically significant. All statistical analyses were performed using SPSS version 26.0, and P-values were reported where applicable.

Clinical validation

Clinical validation included five patients who underwent artificial dermal scaffold reconstruction at the Department of Burn and Plastic Surgery, The First Affiliated Hospital of Soochow University, between August 2024 and August 2025 (Ethics No.: 2026-265). The cohort comprised two men and three women aged 28-72 years (mean, 49.20 ± 17.91 years). One patient had a scalp defect and four had lower-extremity defects, with dimensions ranging from 1 cm × 1 cm to 34 cm × 39 cm. Causes included traffic-related trauma (n = 1), machinery-related injury (n = 2), chronic ulceration (n = 1), and burns (n = 1). All wounds exposed bone, tendon, or another deep structure. Each patient underwent debridement, negative-pressure wound therapy as clinically indicated, implantation of a bilayer Lando scaffold, and subsequent split-thickness autografting. The institutional ethics committee waived the requirement for written informed consent because this retrospective study used existing, de-identified clinical images and biopsy data, posed minimal risk to patients, and did not interfere with routine care.

SS-OCT imaging was performed on approximately postoperative days 2, 7, and 14, and the images were compared with H&E staining and CD34 immunohistochemistry from the same time points. Three wound sites were selected, and three volumes were acquired per site. Photographs were used to relocate these sites during follow-up. Biopsy specimens obtained on days 2, 7, and 14 were evaluated using H&E staining and CD34 immunohistochemistry. For volume-based assessment, V_0 was defined as the baseline collagen sponge volume immediately after scaffold implantation on the day of surgery (postoperative day 0), and V_t as the segmented collagen sponge volume at each subsequent follow-up. IRDR (%) was calculated as $(V_0 - V_t) / V_0 \times 100$[24]. Intraoperative or postoperative day 0 OCT acquisition was not feasible in this clinical cohort. Therefore, V_0 was estimated from the manufacturer-provided baseline three-dimensional geometric parameters of the implanted Lando scaffold rather than measured by OCT. Without day-0 OCT imaging, the true *in vivo* baseline volume could not be determined. The manufacturer-derived volume may differ from the actual implanted volume because of trimming, hydration, compression, wound geometry, fixation, and tissue swelling. Consequently, non-zero IRDR values on postoperative day 2 cannot be attributed solely to scaffold degradation; they may partly reflect differences between the nominal and actual implanted volumes. Clinical values are therefore reported as "estimated IRDR" and should be interpreted as a relative longitudinal index rather than an absolute volumetric measure. Future studies should obtain an immediate postoperative or day-0 OCT measurement whenever feasible.

Histological processing and immunohistochemistry

Harvested wound tissues were fixed in 4% paraformaldehyde for 24 h, dehydrated through a graded ethanol series, and embedded in paraffin. Sections were cut at a thickness of 5 μm. For H&E staining, deparaffinized sections were stained with H&E using standard histological protocols. For CD31 and CD34 immunohistochemistry, antigen retrieval was performed in citrate buffer (pH 6.0) under high-pressure heating. Sections were blocked with 5% bovine serum albumin at room temperature for 30 min to reduce nonspecific binding, then incubated overnight at 4 °C with primary antibodies against CD31 (Proteintech, 28083-1-AP; dilution, 1:1,000) or CD34 (Proteintech, 14486-1-AP; dilution, 1:1,000). Corresponding secondary antibodies were applied, followed by 3,3'-diaminobenzidine (DAB) chromogenic development and hematoxylin counterstaining. To quantify CD34-positive microvessels, five random high-power fields (HPFs; 200× magnification) were selected per histological section. For each patient, microvessel numbers from all HPFs across their respective biopsy sections were averaged to generate a single patient-level value. Group mean values and standard deviations were then calculated based on these individual patient-derived averages, with patients treated as independent statistical units. Microvessels were counted manually in each field using ImageJ version 1.54f. In this clinical cohort, biopsy samples were obtained from 5 patients at each postoperative time point. *N* denotes the number of patients in clinical analyses; *n* denotes the number of histological sections or fields of view, as specified in the text and figure legends.

RESULTS

Correlation between OCT and histological findings in the murine wound model

To assess the accuracy of OCT imaging, we compared B-scan images with H&E-stained sections and evaluated angiogenesis by comparing en face OCT images with CD31 immunohistochemistry [Figure 2A]. Mice received Lando artificial dermal scaffolds either with bFGF [Figure 2B] or without bFGF [Figure 2C].

Lando artificial dermal scaffold combined with bFGF

On day 3 in the bFGF-treated group, B-scan images clearly depicted the silicone and collagen sponge layers of the artificial dermal scaffold. Focal, heterogeneous high-scattering spots suggestive of inflammation were observed in the dermal layer. H&E-stained sections showed dermal defects and numerous cavities lined with homogeneous eosinophilic material. Migrating fibroblasts were visible, and inflammatory cells (black arrows) had infiltrated the wound. No dendritic vascular structures were detected in en face images, and no CD31-positive vascular structures were observed in the wound bed. By day 7, the low-signal silicone layer had gradually diminished on B-scans. Small, round, well-defined signal voids, likely representing vascular lumina, and well-demarcated low-scattering areas suggestive of exudate appeared in the dermal layer. H&E-stained sections showed fewer cavities, capillary dilation, widened tissue spaces, and substantial exudate and inflammatory cell infiltration. En face images showed an increase in high-signal dendritic structures, and CD31-positive vascular structures were visible in the central wound area. On day 11, low-scattering areas persisted on B-scans, alongside homogeneous, thickened regions with moderate scattering. H&E-stained sections still contained substantial exudate and inflammatory cells, although both appeared to decrease compared with day 7. More fibroblasts (blue arrows) and newly formed collagen fibers were present within the wound. En face images showed markedly thickened, high-signal dendritic structures, while CD31 immunohistochemistry demonstrated large vascular structures and abundant neovascularization [Figure 2B].

Control group receiving artificial dermal scaffold alone

In the scaffold-only group, B-scan images showed numerous heterogeneous high-scattering spots in the dermal layer. H&E-stained sections showed marked inflammatory cell infiltration. En face images revealed large areas of high signal intensity but no dendritic vascular structures, and no CD31-positive vascular structures were detected in the wound bed. By day 7, the low-signal silicone layer and porous scaffold architecture were no longer visible on B-scans, which instead showed prominent low-scattering regions.

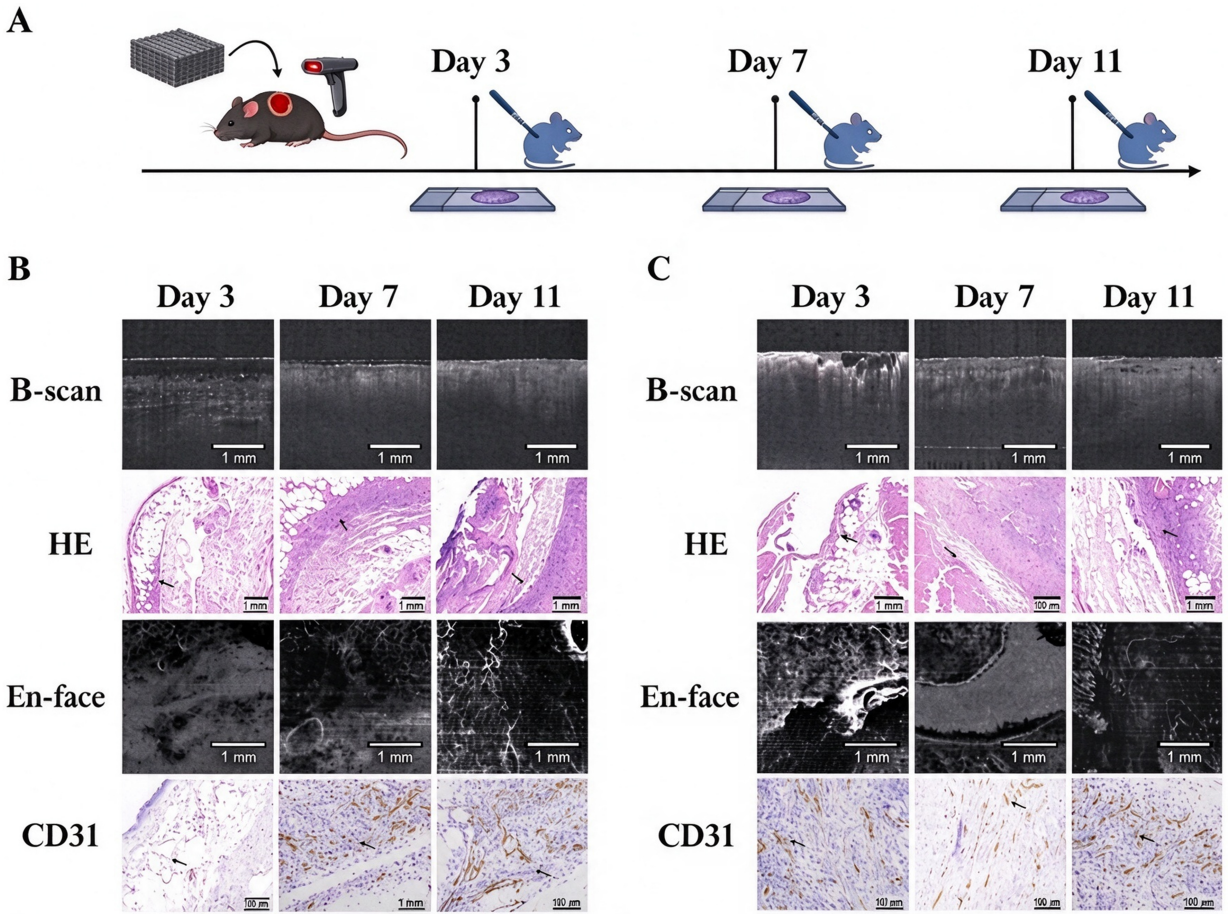


Figure 2. B-scan and en face OCT images, H&E-stained sections, and CD31 immunohistochemistry on postoperative days 3, 7, and 11. (A) Timeline of wound assessment in mice receiving Lando artificial dermal scaffolds; (B) Wounds treated with Lando artificial dermal scaffolds and Beifuji (recombinant bovine basic fibroblast growth factor); (C) Wounds treated with Lando artificial dermal scaffolds alone (control group). B-scan: Brightness scan; OCT: optical coherence tomography; H&E: hematoxylin and eosin; CD31: cluster of differentiation 31.

H&E-stained sections revealed markedly widened tissue spaces, substantial exudate, and inflammatory cell infiltration. En face images showed extensive pus-like signals without clear branching structures. Similarly, no distinct CD31-positive vascular structures were evident in the wound. On day 11, the low-scattering regions on B-scans had diminished and were replaced by homogeneous, thickened regions with moderate scattering. H&E-stained sections showed exudate, inflammatory cells, and fibroblasts within the wound. En face images revealed high-signal branching vascular structures, while CD31 immunohistochemistry demonstrated appreciable neovascularization [Figure 2C].

Longitudinal OCT imaging and digital photography of scaffold-treated murine wounds

Wound healing was monitored using OCT and digital photography on postoperative days 3, 5, 7, 9, and 11 [Figure 3A]. Figure 3 shows the treatment protocol and corresponding OCT images for mice receiving Lando artificial dermal scaffolds with Beifuji (recombinant bovine bFGF; Figure 3B) or scaffolds alone (control group; Figure 3C).

Control group with artificial dermal scaffold alone

In the control group [Figure 3C], en face OCT images on day 3 showed dense vascular structures in some areas of normal skin, while the porous, grid-like texture of the scaffold remained clearly visible. By day 7, a few vascular signals had appeared in the upper-left corner of the image. Meanwhile, the overall signal

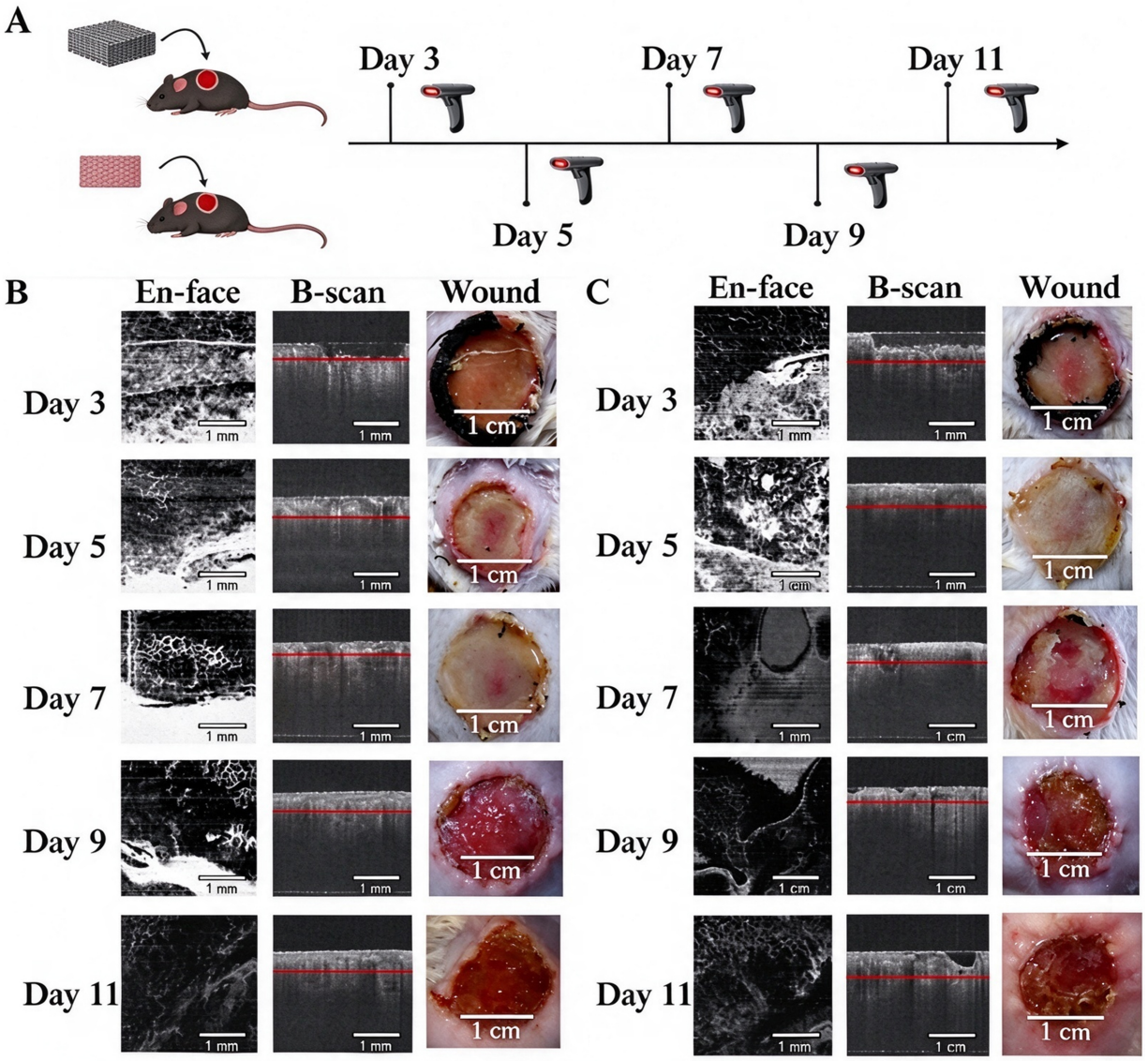


Figure 3. En face OCT images, corresponding B-scans, and macroscopic wound photographs on postoperative days 3, 5, 7, 9, and 11. (A) Experimental protocol for wound creation and implantation of Lando artificial dermal scaffolds or autologous skin grafts in mice; (B) Wounds treated with Lando artificial dermal scaffolds and Beifuji (recombinant bovine basic fibroblast growth factor); (C) Wounds treated with Lando artificial dermal scaffolds alone (control group). Red lines on the B-scans indicate the depth at which the en face images were generated. B-scan: Brightness scan; OCT: optical coherence tomography.

intensity of the scaffold layer gradually decreased, its initially regular architecture became blurred, and signals resembling purulent material emerged. On day 11, the scaffold area was progressively covered by a new, high-signal epidermal layer. Corresponding B-scans showed partial detachment of the silicone layer in some regions as early as day 3. By day 7, vascular structures appeared denser at the wound edges than in the center. Irregular punctate or short linear hyperreflective foci gradually developed within the scaffold layer, while the layer became thinner and its overall reflectivity decreased as degradation progressed. Macroscopic photographs at the corresponding time points showed bubbles within the central red area on postoperative day 3. By day 7, most of the scaffold had detached. On day 11, the scaffold began to integrate with the wound bed, and the wound surface became drier.

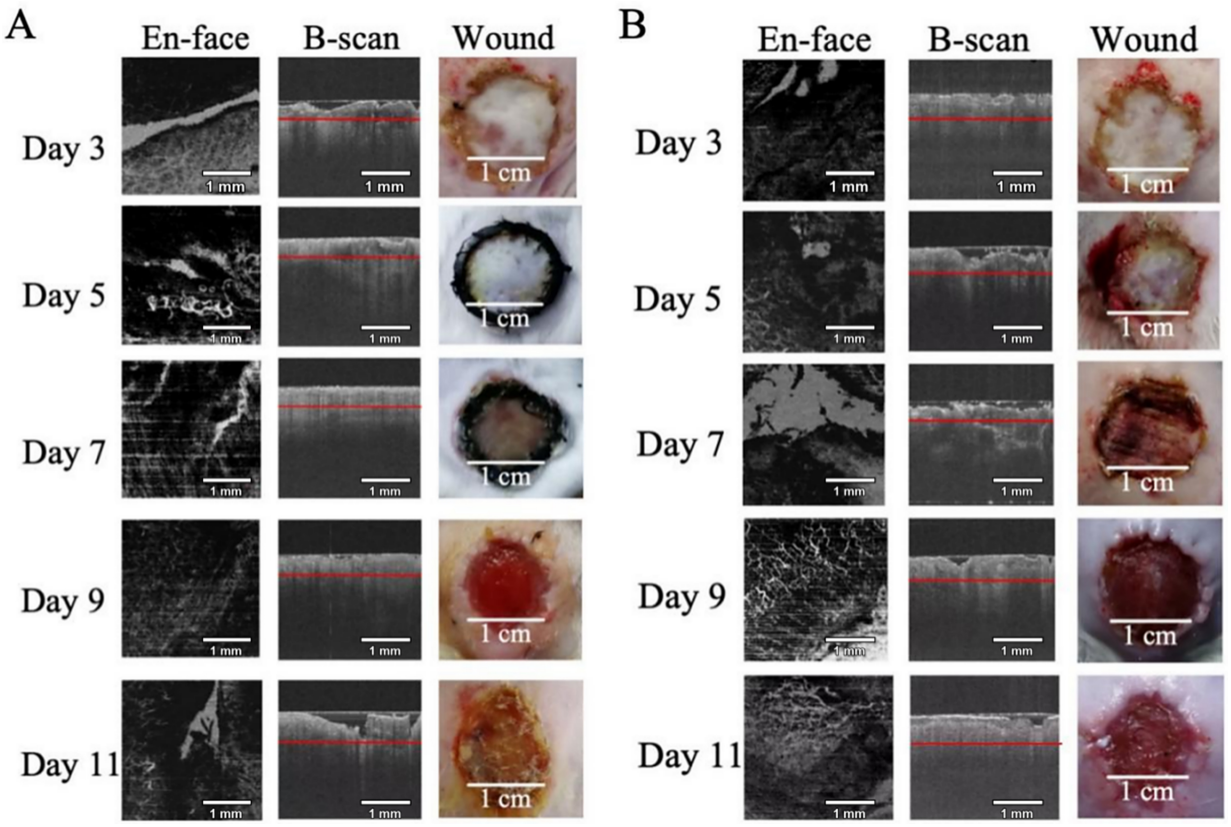


Figure 4. En face OCT images, corresponding B-scans, and macroscopic wound photographs on postoperative days 3, 5, 7, 9, and 11. (A) Wounds treated with autologous skin grafts and Beifuji (recombinant bovine basic fibroblast growth factor); (B) Wounds treated with autologous skin grafts alone (control group). Red lines on the B-scans indicate the depth at which the en face images were generated. B-scan: Brightness scan; OCT: optical coherence tomography.

Artificial dermal scaffold with bFGF

In the combined treatment group [Figure 3B], en face OCT images clearly showed the porous, grid-like texture of the scaffold immediately after implantation. From day 5, neovascularization extended from the wound edges toward the scaffold center, appearing as network-like or dendritic high-signal structures that progressively increased in density. From day 7 onward, the scaffold layer became thinner, its overall signal intensity decreased, and its initially regular architecture became blurred. Concurrently, superficial en face images showed centripetal migration of the regenerating epidermis, which progressively covered the scaffold as a new, high-signal layer. In the early postimplantation phase, corresponding B-scans showed a continuous, homogeneous scaffold band with moderate-to-high reflectivity. As cellular infiltration and vascularization progressed, irregular punctate or short linear hyperreflective foci appeared within the initially uniform scaffold layer, suggesting the ingrowth of cells and nascent vessels. The scaffold layer also became thinner and less reflective, indicating ongoing degradation. Macroscopic photographs showed a translucent dermal scaffold on postoperative day 3, through which underlying native murine tissue was visible, without apparent granulation tissue formation. As healing progressed, wound exudate was present, and scaffold transparency increased. On days 9 and 11, integration with the wound bed improved, and the wound surface became drier. By day 11, fusion between the wound periphery and the scaffold collagen layer was evident, and the overlying silicone layer showed signs of impending detachment.

OCT findings in wounds treated with autologous skin grafts

Figure 4 presents wound changes and corresponding OCT images after autologous skin grafting with or without bFGF (Beifuji). Mice received autologous skin grafts with bFGF [Figure 4A] or grafts alone [Figure 4B].

Autologous skin grafts with bFGF

In the bFGF-treated group [Figure 4A], early en face OCT images showed sparse dendritic vascular structures and pus-associated signals with a low signal-to-noise ratio at the wound edges. On day 7, thicker branching vascular signals were visible in non-purulent areas. Vascular proliferation was evident by day 11, when vascular density appeared markedly increased in the sampled marginal regions. Corresponding B-scans showed increased dermal signal intensity after grafting, poor graft adhesion, and flocculent areas of moderate-to-high reflectivity in the subcutaneous layer. Macroscopic photographs showed that the graft had survived and adhered to the wound bed by day 5, although it appeared dry, hardened, and poorly integrated. Tissue fluid and blood exudation were observed during sampling, and the subcutaneous wound area showed signs of infection and pus formation. From day 9, the graft was gradually debrided, and the wound bed showed signs of drying by day 11.

Autologous skin grafts alone

No additional notable findings were recorded in the group receiving autologous skin grafts without bFGF [Figure 4B].

Clinical validation

The clinical cohort included five patients: one with a scalp wound and four with lower-extremity wounds. All underwent reconstruction using artificial dermal scaffolds. To evaluate the clinical applicability of SS-OCT, wound biopsies for H&E staining and CD34 immunohistochemistry were collected on postoperative days 2, 7, and 14, with SS-OCT imaging performed at the same time points. Figure 5A-C presents the corresponding assessments on days 2, 7, and 14, respectively: (i) H&E-stained sections; (ii) CD34 immunohistochemistry; (iii) three-dimensional reconstructions of the collagen sponge layer; (iv) B-scan OCT images; and (v) en face OCT images.

On postoperative day 2, H&E staining showed an intact, well-defined scaffold architecture. ImageJ analysis of CD34-stained sections detected no microvessels within the scaffold matrix in high-power fields (HPFs). Corresponding B-scans showed a clear boundary between the lower surface of the collagen sponge layer and the underlying wound bed, consistent with minimal degradation during this early phase. Matched en face images showed regularly arranged circular pores without detectable vascularization. On day 7, H&E staining clearly delineated the sponge collagen framework, with sparse deposition of new collagen and extensive cellular infiltration throughout the matrix. CD34 staining yielded a microvessel count of 3.6 ± 2.0 per HPF. Values represent mean microvessel counts per high-power field (HPF), calculated from patient-level averaged values. B-scans showed a less compact collagen sponge layer containing numerous cystic voids. Corresponding en face images showed pore collapse and a transition from regular circular pores to irregular cavities, attributed primarily to spontaneous biodegradation of the collagen sponge. Early vascularization was visible at the wound periphery. On day 14, H&E staining showed abundant newly synthesized collagen fibers filling the wound bed, while the original sponge collagen framework was no longer distinguishable. CD34 immunohistochemistry showed a marked increase in microvessel density to 39.3 ± 5.5 per HPF. Values represent mean microvessel counts per high-power field (HPF), calculated from patient-level averaged values. B-scans showed large dark voids resulting from advanced scaffold degradation. Corresponding en face images showed substantial matrix loss, with extensive degradation-related defects completely replacing the original circular pores. The collagen sponge layer was markedly thinner than in the early postoperative period. This thinning accompanied endogenous collagen production and progressive vascular ingrowth, which generated dermal-like tissue that infiltrated and replaced the deeper portion of the collagen sponge. Extensive vascularization was visible at both the wound margin and center on day 14.

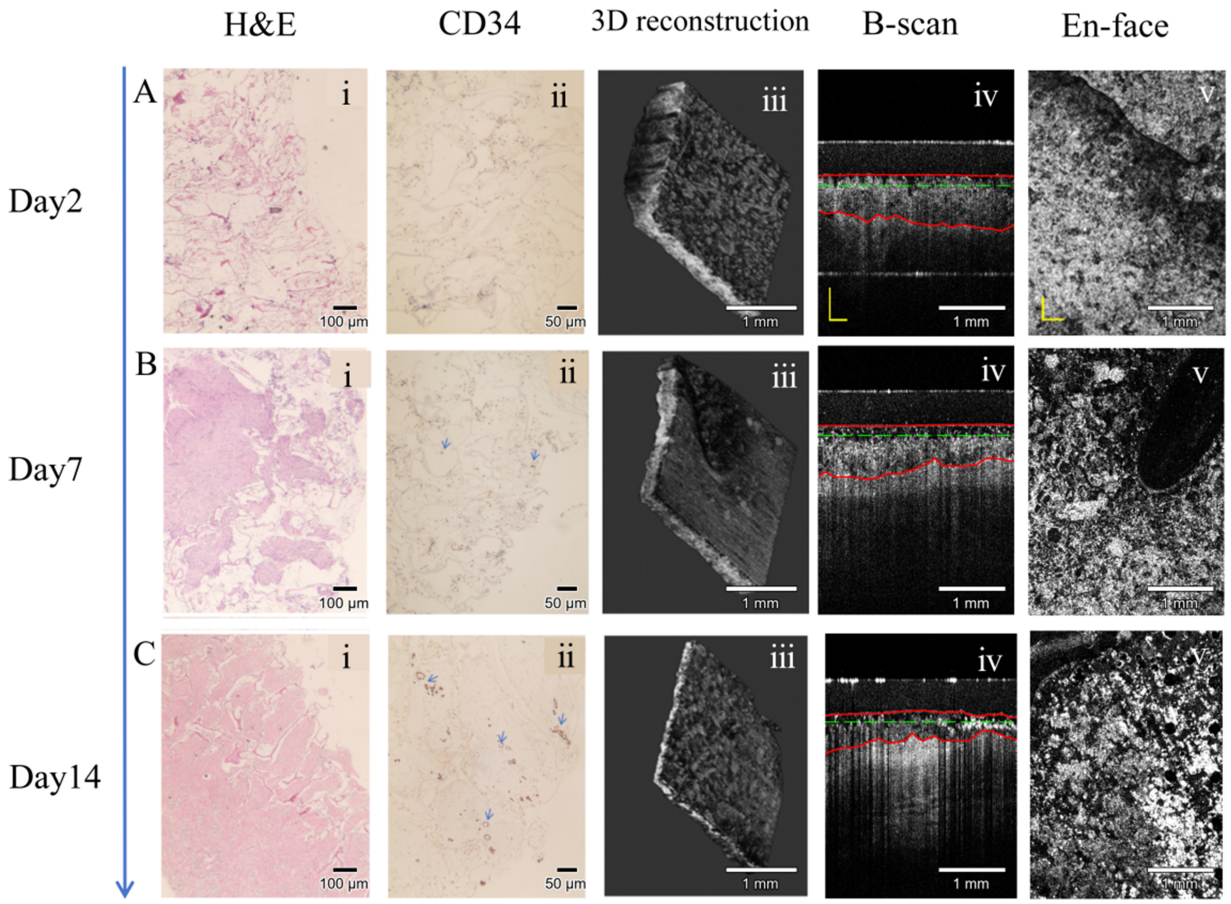


Figure 5. Representative clinical validation images obtained on postoperative days 2 (A), 7 (B), and 14 (C): (i) H&E-stained histological sections; (ii) CD34 immunohistochemistry; (iii) three-dimensional reconstructions of the collagen sponge layer; (iv) B-scan OCT images; and (v) en face OCT images. H&E: Hematoxylin and eosin; CD34: cluster of differentiation 34; OCT: optical coherence tomography; B-scan: brightness scan.

Table 1. Longitudinal estimated IRDR values in patients after artificial dermal-scaffold implantation

Time point (Day)	Mean IRDR (%)	Standard deviation (SD)	Variance
2	8	2	4
7	28	8.4	70.56
14	56	16.8	282.24

Data are presented as mean ± standard deviation. Paired-samples *t*-tests were used for pairwise comparisons between different postoperative time points. IRDR: Index of Scaffold Ingrowth, Vascularization and Degradation; SD: standard deviation.

H&E staining documented progressive scaffold biodegradation, cellular infiltration, new collagen deposition, and microvascular ingrowth. Quantitative analysis of CD34 immunohistochemistry using ImageJ demonstrated changes in neovascularization within the scaffold over time. The collagen sponge regions outlined in red on B-scans [Figure 5A-C (iv)] became progressively thinner, and the interface between the lower scaffold surface and native tissue became less distinct. These changes reflected progressive tissue integration, adherence, and matrix degradation at the graft-host interface. En face OCT images [Figure 5A-C (v)] showed continued enlargement of dark, pore-like cavities alongside expansion of continuous, sheet-like regions with high grayscale intensity, representing regenerated skin tissue. Vascularization increased steadily as microvessels extended from the wound periphery toward the center.

Estimated IRDR values were calculated for all five patients on postoperative days 2, 7, and 14 using the predefined formula [Table 1].

Paired-samples *t*-tests were used to compare estimated IRDR values between postoperative days 2 and 7 ($P = 0.0042$), days 7 and 14 ($P = 0.0126$), and days 2 and 14 ($P = 0.0025$). Estimated IRDR values increased progressively from day 2 to day 14, with a sustained upward linear trend. Between-patient variability increased over time, which was attributed to differences in scaffold biodegradation and vascular ingrowth. Values were non-zero on day 2 because V_0 represented the theoretical scaffold volume at implantation on day 0, whereas the first *in vivo* OCT measurement was obtained on day 2. As noted in the Methods, this difference may reflect both early scaffold degradation and discrepancies between nominal and actual implanted volumes.

DISCUSSION

In the murine experiment, multimodal OCT imaging, including B-scan and en face imaging, was combined with H&E staining and CD31 immunohistochemistry to characterize three main stages of full-thickness wound repair: inflammation, proliferation, and early remodeling[25]. The scaffold-treated mice received either Lando artificial dermal scaffolds alone or scaffolds supplemented with bFGF.

The close correspondence between OCT features and histopathological findings supports the use of OCT for non-invasive wound assessment. Heterogeneous high-scattering spots on B-scans corresponded to inflammatory cell infiltration on H&E-stained sections, while well-demarcated low-scattering regions corresponded to widened tissue spaces and fluid accumulation. The emergence of high-signal dendritic structures on en face OCT coincided with the appearance of CD31-positive microvessels[26]. The gradual reduction in scaffold signal intensity and thickness on OCT paralleled the cellular infiltration and biodegradation observed histologically.

Longitudinal OCT imaging captured the progression of wound healing in a manner consistent with established histological phases. During the early postoperative period (days 3-7), heterogeneous high-scattering spots within the scaffold and dermal layer corresponded to inflammatory cell infiltration. From day 7 onward, high-signal dendritic structures progressively emerged and increased in density from the wound edges toward the center, corresponding to CD31-positive neovascularization. Concurrently, B-scans showed a gradual loss of regular scaffold architecture and the appearance of punctate signal voids, consistent with vascular ingrowth and scaffold remodeling[20,24,27].

The two scaffold groups showed different healing trajectories. Compared with the scaffold-only group, the Lando + bFGF group showed earlier and more pronounced angiographic signals, more orderly scaffold integration and degradation on B-scans, and fewer persistent low-scattering regions. These observations suggest that bFGF promoted vascular ingrowth and the transition from inflammation to proliferation[7,28]. However, the small group sizes mean that these comparisons should be interpreted descriptively. The ability of OCT to display treatment-related structural and vascular changes over time nevertheless supports its potential use in monitoring wounds and assessing the timing of subsequent treatment.

In the clinical cohort, the *in vivo* behavior of artificial dermal scaffolds was assessed by comparing SS-OCT B-scan and en face images with H&E staining and CD34 immunohistochemistry. SS-OCT findings were closely consistent with histological changes in the wound bed. Estimated IRDR values for the collagen sponge layer increased progressively during follow-up, suggesting that this index may be useful for longitudinal OCT assessment of scaffold degradation. Larger studies are needed to establish its performance as a clinical biomarker. These findings further support the feasibility of SS-OCT for non-invasive longitudinal monitoring of implanted artificial dermal scaffolds[29]. The increase in estimated IRDR over time is consistent with the remodeling pattern reported by Chen *et al.*[24] and with previous human studies combining OCT and histological assessment during skin substitute-mediated wound repair[30]. Together, the

murine and clinical findings support the use of SS-OCT to monitor artificial dermal scaffold integration non-invasively *in situ*. Compared with conventional observational methods, OCT may reduce reliance on subjective assessment and delays associated with histological evaluation, providing a practical tool to support individualized wound management after dermal scaffold reconstruction[31].

Several limitations should be considered. The murine groups were small, and OCT sampled only selected sites within heterogeneous wounds. In the murine bFGF experiment, treated mice received repeated perilesional injections, whereas controls received no intervention. The injection procedure may therefore have confounded the results, and differences in wound remodeling cannot be attributed entirely to bFGF. The clinical component was conducted at a single center without a parallel control group and included only five patients with substantial variation in wound size and etiology. Comparisons between SS-OCT and histopathology were predominantly visual and qualitative; the small sample size precluded formal quantitative analyses of agreement, correlation, and reproducibility. Larger prospective studies are needed to evaluate agreement between IRDR and histological measures and establish its clinical utility. The relationship between individual IRDR values and histological vascular measurements also requires validation, while histological sampling after grafting was limited to avoid additional injury. Motion, probe pressure, optical coupling, and wound exudate may affect OCT contrast. Future studies should standardize imaging-site relocation and probe pressure, use blinded image assessment, evaluate segmentation reproducibility, and prospectively compare OCT-derived indicators with clinical and histological outcomes[32,33].

Conclusion

The portable 1,060 nm SS-OCT system enabled non-invasive, depth-resolved visualization of artificial dermal scaffold apposition, structural remodeling, and vascular patterns. In mice, OCT findings corresponded to changes observed with H&E staining and CD31 immunohistochemistry during wound healing. In patients, serial OCT findings were consistent with H&E staining and CD34 immunohistochemistry. These results suggest that SS-OCT can provide longitudinal information on scaffold integration and may help assess wound status, inform dressing-change intervals, and guide the timing of second-stage skin grafting. Larger prospective studies are needed to confirm these applications.

DECLARATIONS

Authors' contributions

Conceptualization, methodology, animal experiment, manuscript writing: Ren Z
Data curation, image analysis, statistical analysis: Tang S
Animal surgery, sample collection: Xu Y
OCT system operation, data acquisition: Cui Y
OCT hardware and algorithm design: Mo J
Project supervision, funding acquisition, manuscript revision: Li K
All authors read and approved the final manuscript and agree to be accountable for all aspects of the work.

Availability of data and materials

The datasets generated and analyzed during the current study are available from the corresponding author upon reasonable request.

AI and AI-assisted tools statement

During the preparation of this manuscript, OpenAI Codex (model: GPT-5.6 Sol; released 2026-07-09; accessed 2026-08-30) was used solely to assist in creating the handheld optical coherence tomography (OCT) probe illustration included as one element of the graphical abstract. The tool did not influence the language editing, study design, data collection, analysis, interpretation, or the scientific content of the work. All authors take full responsibility for the accuracy, integrity, and final content of the manuscript.

Financial support and sponsorship

This study was supported by the Suzhou Municipal Health Commission (MSXM2025002), the Suzhou Municipal Bureau of Science and Technology (SSD2024052), and the Suzhou Municipal Bureau of Science and Technology (SKYD2023104). The funders had no role in study design, data collection, analysis, or interpretation; manuscript preparation; or the decision to submit the work for publication.

Conflicts of interest

All authors have declared that there are no conflicts of interest.

Ethical approval and consent to participate

All animal experiments were approved by the Animal Ethics Committee of Soochow University (Ethics No. SUDA20250415A01) and complied with the ARRIVE 2.0 guidelines. The clinical study was approved by the Ethics Committee of the First Affiliated Hospital of Soochow University (Ethics No. 2026-265). This approval covers the retrospective analysis of clinical data collected from August 2024 to August 2025, including patient enrolment, serial SS-OCT imaging, wound biopsy, and histopathological analyses. The requirement for written informed consent was waived by the ethics committee. The waiver was granted because this retrospective study used de-identified existing clinical image and biopsy data, imposed minimal risk to patients, and did not interfere with routine clinical care.

Consent for publication

Not applicable.

Copyright

© The Author(s) 2026.

REFERENCES

1. Gurtner GC, Werner S, Barrandon Y, Longaker MT. Wound repair and regeneration. *Nature.* 2008;453:314-21. DOI PubMed
2. Wang Y, Beekman J, Hew J, et al. Burn injury: challenges and advances in burn wound healing, infection, pain and scarring. *Adv Drug Deliv Rev.* 2018;123:3-17. DOI PubMed
3. Kruse-Lösler B, Presser D, Meyer U, Schul C, Luger T, Joos U. Reconstruction of large defects on the scalp and forehead as an interdisciplinary challenge: experience in the management of 39 cases. *Eur J Surg Oncol.* 2006;32:1006-14. DOI PubMed
4. Ryssel H, Gazyakan E, Germann G, Ohlbauer M. The use of MatriDerm in early excision and simultaneous autologous skin grafting in burns--a pilot study. *Burns.* 2008;34:93-7. DOI PubMed
5. Eming SA, Martin P, Tomic-Canic M. Wound repair and regeneration: mechanisms, signaling, and translation. *Sci Transl Med.* 2014;6:265sr6. DOI PubMed PMC
6. Taylor BC, Triplet JJ, Wells M. Split-thickness skin grafting: a primer for orthopaedic surgeons. *J Am Acad Orthop Surg.* 2021;29:855-61. DOI PubMed
7. Veith AP, Henderson K, Spencer A, Sligar AD, Baker AB. Therapeutic strategies for enhancing angiogenesis in wound healing. *Adv Drug Deliv Rev.* 2019;146:97-125. DOI PubMed PMC
8. Corrêa FB, Castro JCD, Almeida IR, Farina-Junior JA, Coltro PS. Evaluation of contraction of the split-thickness skin graft using three dermal matrices in the treatment of burn contractures: a randomised clinical trial. *Wound Repair Regen.* 2022;30:222-31. DOI PubMed
9. Chattopadhyay S, Raines RT. Collagen-based biomaterials for wound healing. *Biopolymers.* 2014;101:821-33. DOI PubMed PMC
10. Jeschke MG, van Baar ME, Choudhry MA, Chung KK, Gibran NS, Logsetty S. Burn injury. *Nat Rev Dis Primers.* 2020;6:11. DOI PubMed PMC
11. Lin YN, Wang YC, Lee SS, et al. The bridging effect of artificial dermis on reconstruction of skin avulsion injury. *Int J Low Extrem Wounds.* 2025;24:1140-7. DOI PubMed
12. Romano G, Bouaoud J, Moya-Plana A, Benmoussa N, Honart JF, Leymarie N. Integra® dermal regeneration template for full thickness carcinologic scalp defects: our 6 years' experience retrospective cohort and literature review. *J Stomatol Oral Maxillofac Surg.* 2021;122:256-62. DOI PubMed
13. Limandjaja GC, Niessen FB, Scheper RJ, Gibbs S. Hypertrophic scars and keloids: overview of the evidence and practical guide for differentiating between these abnormal scars. *Exp Dermatol.* 2021;30:146-61. DOI PubMed PMC
14. van den Bosch AS, Verwilligen RAF, Pijpe A, et al. ; National Burn Care, Education & Research group, The Netherlands. Outcomes of dermal substitutes in burns and burn scar reconstruction: a systematic review and meta-analysis. *Wound Repair Regen.* 2024;32:960-78. DOI PubMed PMC

15. Tottoli EM, Dorati R, Genta I, Chiesa E, Pisani S, Conti B. Skin wound healing process and new emerging technologies for skin wound care and regeneration. *Pharmaceutics.* 2020;12:735. DOI PubMed PMC
16. Gong P, Es'haghian S, Wood FM, Sampson DD, McLaughlin RA. Optical coherence tomography angiography for longitudinal monitoring of vascular changes in human cutaneous burns. *Exp Dermatol.* 2016;25:722-4. DOI PubMed
17. Huang D, Swanson EA, Lin CP, et al. Optical coherence tomography. *Science.* 1991;254:1178-81. DOI PubMed PMC
18. Ai Ping Yow, Jun Cheng, Annan Li, et al. Automated in vivo 3D high-definition optical coherence tomography skin analysis system. *Annu Int Conf IEEE Eng Med Biol Soc.* 2016;2016:3895-8. DOI PubMed
19. Deegan AJ, Wang W, Men S, et al. Optical coherence tomography angiography monitors human cutaneous wound healing over time. *Quant Imaging Med Surg.* 2018;8:135-50. DOI PubMed PMC
20. Moiemen NS, Vlachou E, Staiano JJ, Thawy Y, Frame JD. Reconstructive surgery with Integra dermal regeneration template: histologic study, clinical evaluation, and current practice. *Plast Reconstr Surg.* 2006;117:160S-74. DOI PubMed
21. Park KS, Choi WJ, Song S, Xu J, Wang RK. Multifunctional in vivo imaging for monitoring wound healing using swept-source polarization-sensitive optical coherence tomography. *Lasers Surg Med.* 2018;50:213-21. DOI PubMed PMC
22. Bouma BE, de Boer JF, Huang D, et al. Optical coherence tomography. *Nat Rev Methods Primers.* 2022;2:79. DOI PubMed PMC
23. Popescu DP, Choo-Smith LP, Flueraru C, et al. Optical coherence tomography: fundamental principles, instrumental designs and biomedical applications. *Biophys Rev.* 2011;3:155. DOI PubMed PMC
24. Chen Z, Cheng Q, Wang L, Mo Y, Li K, Mo J. Optical coherence tomography for in vivo longitudinal monitoring of artificial dermal scaffold. *Lasers Surg Med.* 2023;55:316-26. DOI PubMed
25. Iqbal MZ, Riaz M, Biedermann T, Klar AS. Breathing new life into tissue engineering: exploring cutting-edge vascularization strategies for skin substitutes. *Angiogenesis.* 2024;27:587-621. DOI PubMed PMC
26. Schuh S, Berger M, Schiele S, et al. Dynamic optical coherence tomography for imaging acute wound healing. *Int Wound J.* 2024;21:e70015. DOI PubMed PMC
27. Li Y, Sakamoto M, Matsuno K, et al. Potential of gelatin hydrogel nonwoven fabrics (Genocel) as a skin substitute in a diabetic mouse skin defect model. *Regen Ther.* 2024;27:482-7. DOI PubMed PMC
28. Diemer M, Strauß S, Bucan V, et al. Vascularization potential of a dermal skin substitute material (Biodegradable Temporizing Matrix) by proangiogenic growth factors and ASC - an in ovo study. *J Mater Sci Mater Med.* 2025;37:6. DOI PubMed PMC
29. Deegan AJ, Lu J, Sharma R, Mandell SP, Wang RK. Imaging human skin autograft integration with optical coherence tomography. *Quant Imaging Med Surg.* 2021;11:784-96. DOI PubMed PMC
30. Greaves NS, Iqbal SA, Hodgkinson T, et al. Skin substitute-assisted repair shows reduced dermal fibrosis in acute human wounds validated simultaneously by histology and optical coherence tomography. *Wound Repair Regen.* 2015;23:483-94. DOI PubMed
31. Pappalardo A, Alvarez Cespedes D, Fang S, et al. Engineering edgeless human skin with enhanced biomechanical properties. *Sci Adv.* 2023;9:eade2514. DOI PubMed PMC
32. Jorgensen AM, Gorkun A, Mahajan N, et al. Multicellular bioprinted skin facilitates human-like skin architecture in vivo. *Sci Transl Med.* 2023;15:eadf7547. DOI PubMed
33. Xu Y, Liu Y, Cao P, et al. Effectiveness of double-layer artificial dermis repair material combined with autologous skin patch in repairing deep skin and soft tissue defects: a retrospective study. *J Dermatolog Treat.* 2025;36:2541970. DOI PubMed

Disclaimer/Publisher's Note: All statements, opinions, and data contained in this publication are solely those of the individual author(s) and contributor(s) and do not necessarily reflect those of OAE and/or the editor(s). OAE and/or the editor(s) disclaim any responsibility for harm to persons or property resulting from the use of any ideas, methods, instructions, or products mentioned in the content.

© The Author(s) 2026. Open Access This article is licensed under a Creative Commons Attribution 4.0 International License (https://creativecommons.org/licenses/by/4.0/), which permits unrestricted use, sharing, adaptation, distribution and reproduction in any medium or format, for any purpose, even commercially, as long as you give appropriate credit to the original author(s) and the source, provide a link to the Creative Commons license, and indicate if changes were made.